PAPER

Check for updates

Ultralow thermal conductivity and anharmonic rattling in two-dimensional CrSX (X = Cl, Br, I) monolayers†

Xiaowei Xuan, Zhaoyu Yang, Rui Du, Yimeng Zhao, Yuli Yan, ⓘ Chang Liu, ⓘ Hang Li and Guangbiao Zhang ⓘ *

Using first-principles calculations and Boltzmann transport theory, we investigate the thermoelectric properties of the 2D CrSX (X = Cl, Br, I) family. The ultralow lattice thermal conductivity (κ_l) values of CrSX monolayers along the x-axis at 300 K are 0.624, 0.419, and 0.179 W m^{-1} K^{-1}, respectively, while along the y-axis they are 0.193, 0.158, and 0.093 W m^{-1} K^{-1}. These low values are attributed to the small phonon relaxation time and flat acoustic phonon dispersions of CrSX monolayers, resulting from the extraordinarily strong anharmonicity. Vibrational pattern analysis confirms that the strong anharmonicity in CrSX monolayers arises from the reciprocal vibrations of the X atoms around equilibrium positions, which can be considered as a generalized effective rattling phenomenon. Due to their low lattice thermal conductivity and favorable electrical transport properties, the CrSX monolayers demonstrate optimal *ZT* values of 1.33 (5.23), 1.18 (5.84), and 2.13 (5.22) along the x-axis (y-axis) at 300 K, respectively. This work not only highlights the significance of rattling modes in driving phonon anharmonicity but also provides valuable insights for discovering and designing thermoelectric materials with ultralow lattice thermal conductivity and high conversion efficiency.

1 Introduction

Thermoelectric (TE) technology is a promising solution to energy issues, as it enables direct or reversible conversion between electrical energy and thermal energy. The energy conversion efficiency of thermoelectric materials is expressed by the dimensionless parameter *ZT*:[1,2]

$$ZT = \frac{S^2 \sigma T}{\kappa_e + \kappa_l},\qquad(1)$$

where S, σ, T, κ_e and κ_l are the Seebeck coefficient, electrical conductivity, absolute temperature, electronic thermal conductivity, and lattice thermal conductivity, respectively. The power factor PF $= S^2\sigma$ determines the ability to generate useful electrical energy at a given temperature difference,[3] and the higher the *ZT* value, the higher the thermoelectric conversion efficiency. Therefore, high-performance TE materials require a high $S^2\sigma$ value and low thermal conductivity. The thermoelectric parameters S, σ and κ_e are highly coupled, which makes it challenging to optimize independently and improve the thermoelectric conversion

Institute for Computational Materials Science, School of Physics and Electronics, International Joint Research Laboratory of New Energy Materials and Devices of Henan Province, Henan University, Kaifeng 475004, China.
E-mail: gbzhang@vip.henu.edu.cn

† Electronic supplementary information (ESI) available. See DOI: https://doi.org/10.1039/d3ma00409k

efficiency.[4–6] Consequently, there are two main approaches to improve *ZT*. The first is to optimize the power factor PF *via* band structure engineering[7,8] and nanostructure design.[9–11] The second is to minimize the lattice thermal conductivity κ_l through anharmonic lattices,[12,13] reduced structural dimensionality,[14–16] or by seeking out compounds that feature inherently low κ_l due to van der Waals (vdW) interactions or rattling atoms.[17] Rattling has emerged as an influential and successful strategy to achieve low lattice thermal conductivity. This has led to the discovery of novel materials, including clathrates and filled skutterudites.[18–21] The rattling atoms can scatter heat-carrying phonons from the host lattice, thereby resulting in a lower κ_l while maintaining electronic and electron transport properties.[20] Additionally, rattling systems commonly exhibit large atomic displacement parameters (large mean square displacement) and flat potential energy curves, which have been used to characterize this behavior.[22]

Since the experimental synthesis of graphene, 2D semiconductors have been the focus of thermoelectric research due to their significant phonon scattering and superior electron transport.[23–27] Jinlan Wang's group predicted that the CrSX (X = Cl, Br, I) monolayers are ferromagnetic semiconductors with a moderate band gap, a flat phonon dispersion curve, and superior carrier mobility.[28] These superior properties have piqued our interest in studying the thermoelectric properties of CrSX monolayers. This paper systematically investigates the thermoelectric properties of CrSX monolayers using first

principles calculations and Boltzmann transport theory. We report the extremely low κ_l values of 0.624, 0.419, and 0.179 W m^{-1} K^{-1} in the x-axis and 0.193, 0.158, and 0.093 W m^{-1} K^{-1} in the y-axis at 300 K, respectively. The strong ionic bonds between X and Cr atoms restrict the vibration of X atoms in the Cr–X–Cr plane but allow it in the perpendicular direction. X atoms vibrate back and forth near their equilibrium positions, resembling water plants. This differs from classical rattling, which features flat acoustic phonon modes intersecting with optical modes, although it has similar physical properties, specifically the fact that certain atoms vibrate more frequently than others. The rattling of X atoms scatters the heat-carrying acoustic phonons, resulting in extremely low κ_l. Additionally, we find that CrSX monolayers possess favorable thermoelectric properties, with optimum ZT values of 1.33 (5.23), 1.18 (5.84) and 2.13 (5.22) in the x (y) directions at 300 K, revealing their promising potential as thermoelectric materials. The results indicate that CrSX monolayers exhibit excellent thermoelectric properties and are promising candidate materials for thermoelectric applications.

2 Computational details

We performed simulations of CrSX monolayers using the Vienna Ab Initio Simulation Program (VASP)[29] within the Density Functional Theory (DFT) framework, implementing the Projector Augmented Wave (PAW) method.[30] The exchange correlation energy was handled by the Perdew–Burke–Ernzerhof (PBE) functional under Generalized Gradient Approximation (GGA).[31] The electron correlation effect for the localized 3d orbitals of Cr atoms was treated by an effective on-site Hubbard term U of 3 eV.[28] The plane-wave expansion cutoff energy was 450 eV. The Brillouin zone was sampled using a converged Γ-centered 15 × 13 × 1 k mesh for geometry optimization and electronic structure calculations. The residual force on each atom was less than 1 × 10^{-2} eV Å^{-1}, and the convergence criterion for the total energy was 1 × 10^{-8} eV. A vacuum space is 15 Å to avoid interlayer interactions, and the Heyd–Scuseria–Ernzerhof (HSE06) hybrid functional is used to obtain a more accurate bandgap.[32]

We utilized the Phonopy code[33] with the finite-displacement method[34] to compute the second-order interatomic force constants (IFCs).[33] The ShengBTE code,[35] based on the Boltzmann transport equation, was used to determine the phonon transport properties. Third-order anharmonic IFCs were calculated using the finite-difference method, considering the interaction among 12th-neighbor atoms. The second-order (harmonic) and third-order (anharmonic) IFCs were obtained using 5 × 4 × 1 supercells with 2 × 2 × 1 k-meshes. Phonon momenta q meshes for CrSCl, CrSBr, and CrSI monolayers were 90 × 65 × 1, 87 × 65 × 1, and 83 × 65 × 1, respectively, with the scaleboard set to 0.2.

The electrical transport properties are calculated by solving the Boltzmann transport equation with the BoltZTraP code[36] and using 33 × 26 × 1 k-mesh. The total Seebeck coefficients and electrical conductivity by combining the two spin channels:

$$S = \frac{S_\uparrow \sigma_\uparrow + S_\downarrow \sigma_\downarrow}{\sigma_\uparrow + \sigma_\downarrow}, \qquad (2)$$

$$\sigma = \frac{1}{2}(\sigma_\uparrow + \sigma_\downarrow), \qquad (3)$$

where $S_{\uparrow(\downarrow)}$ and $\sigma_{\uparrow(\downarrow)}$ are the spin up (down) Seebeck coefficients and electronic conductivity. The κ_e is determined by the Wiedemann–Franz law[37] $\kappa_e = L\sigma T$, where L is the Lorentz constant. For the degenerate semiconductors, L is obtained as,[36]

$$L = \frac{\pi^2}{3}\left(\frac{k_B}{e}\right)^2, \qquad (4)$$

which is equal to 2.45 × 10^{-8} V^2 K^{-2}.[38]

The lattice thermal conductivity κ_l and electrical conductivity σ of two-dimensional (2D) materials depend on the effective van der Waals thickness d_V along the z-axis, which can be computed using the following expression:

$$d_V = d_1 + d_2 + d_3, \qquad (5)$$

where d_1 represents the thickness of the atomic layer, while d_2 and d_3 correspond to the van der Waals radii of the atoms on the upper and lower surfaces, respectively.

3 Results and discussion

3.1 Phonon spectrum and lattice thermal conductivity

The phonon dispersion curves and phonon density of states (PhDOS) are shown in Fig. 1. CrSX monolayers have six atoms in primitive cells, so there are eighteen phonon branches in the phonon spectrum, and the acoustic and optical branches are highlighted with different colors. The ZA branch represents the out of plane mode, and the TA and LA branches are the
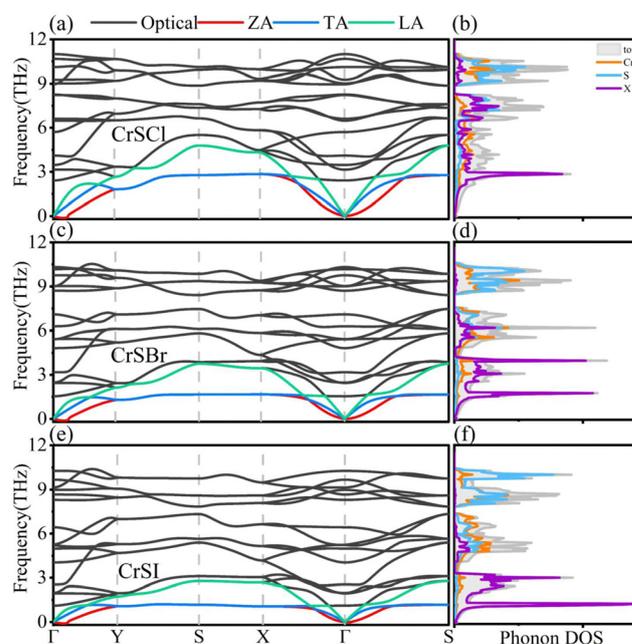

Fig. 1 (a), (c) and (e) Phonon dispersions and (b), (d) and (f) phonon density of states (PhDOS) for CrSX (X = Cl, Br, I).

transverse and longitudinal acoustic modes within the 2D plane,[39] respectively. The slopes of the acoustic branches are much larger than those of the optical branches, predicting that the former carries the larger phonon group velocities and thus makes a major contribution to the κ_l. In the frequency range of the acoustic and low-frequency optical branches, the flat phonon dispersion curves of the ZA and TA branches will lead to small phonon group velocities. Moreover, the LA branch is highly overlapping with the low-frequency optical branches, which demonstrate that acoustic and optical phonons are more easily scattered, resulting in high phonon scattering rates.[40] From Fig. 1(b, d and f), the vibrational modes of X atoms gradually dominate the acoustic region from Cl to I, whereas those of Cr and S atoms dominate the optical region. Overall, the PhDOS of Cr (S) and X exhibit significant mismatch in the acoustic and low-frequency optical branches, indicating the weaker vibrational interactions between Cr (S) and X atoms. This mismatch greatly limits their contribution to the κ_l.[19,41] The flat low-frequency acoustic modes are dominated by vibrations of X atoms, which are the typical of rattling.[21] Hence, based on the available analysis, it can be inferred that CrSX monolayers may have lower κ_l.

The optimized structures of CrSX monolayers are shown in Fig. 2(a and b). Mechanical response is an effective evaluation of the structural stability. The mechanical properties are studied, and the summarized results are presented in Table S2 (ESI†), confirming the stability through the satisfaction of required criteria: $C_{11} > 0$, $C_{33} > 0$, and $C_{11} \times C_{22} > C_{12}^2$.[42–45] The X and Cr atoms form strong ionic bonds, and the X atoms are less likely to vibrate in the Cr–X–Cr plane but more likely to vibrate perpendicular to the Cr–X–Cr plane. The X atoms exhibit effective atomic rattling, resembling water plants that oscillate back and forth around their equilibrium positions. To verify this conclusion, we analyze the atomic displacement parameter (ADP) and potential energy curves. ADP determines the mean square of the displacement amplitudes of atoms around their equilibrium positions.[46–48] Larger ADP values imply more vigorous vibrations, indicating a weak restoring force acting on the vibrating atoms. As shown in Fig. 2(c), the thermally induced ADP of X atoms is significantly larger than those of other atoms, and this effect becomes more pronounced at higher temperatures. Fig. 2(d) describes potential energy as a function of atomic displacement around the equilibrium position for Cr, S, and X atoms in CrSX monolayers. A flatter curve means that less energy is required to leave the equilibrium position,[49] reflecting a weak restoring force on vibrating atoms.[46,50] The potential energy of X atoms is flatter than Cr and S atoms, indicating looser binding in the lattice, consistent with their large ADP values, which indicate weak restoring force on X atoms. The rattling behavior of the X atoms enhances crystal anharmonicity, scatters phonons, and lowers lattice thermal conductivity. The computation of the phonon participation ratio (PR) distinguishes between collective excitations of all atoms and local excitation modes, revealing anharmonic rattling modes in CrSX monolayers and determining the degree of involvement of constituent atoms
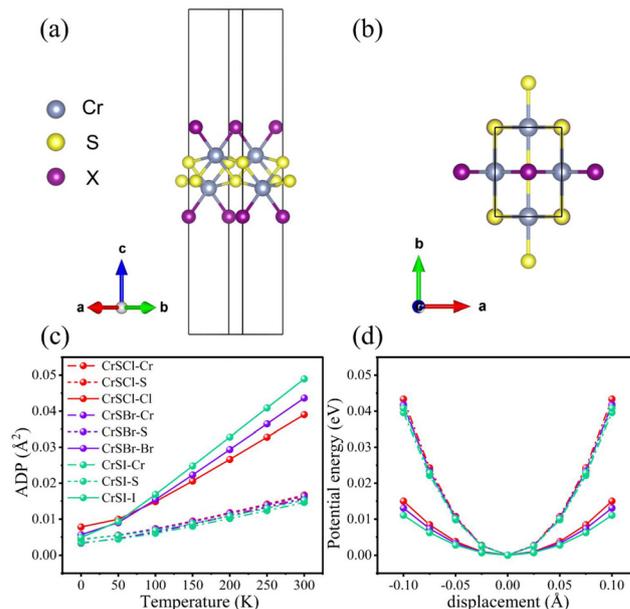

Fig. 2 (a) and (b) are the structures of CrSX monolayers in the top and side views. (c) The atomic displacement parameters (ADPs) for CrSX monolayers. (d) The potential energy curves for Cr, S and X atoms as a function of atomic displacement around the equilibrium positions for CrSX monolayers.

in a specific phonon mode.[51] The PR is defined by the following equation:[52,53]

$$\mathrm{PR}_\lambda = \frac{\left(\sum\limits_{i=1}^{N} \left|u_\lambda^i\right|^2\right)^2}{N\sum\limits_{i=1}^{N} \left|u_\lambda^i\right|^4}, \qquad (6)$$

where N and u_λ^i are the number of atoms in the unit cell and the atomic eigen displacement, respectively. $u_\lambda^i = \varepsilon_\lambda^i \sqrt{M_i}$ is obtained by scaling the phonon eigenvector projected on the ith atom ε_λ^i by the atomic mass M_i. The degree of atom involvement in a given phonon mode λ can be determined by the PR value in the range 0–1, where PR $\sim$ 0 indicates a localized rattling mode while PR $\sim$ 1 represents a propagating vibrational mode with coherent displacements of all atoms.[52,53] In this study, the frequency-resolved PR values of CrSX monolayers are depicted in Fig. 3. The low-frequency range shows similar PR characteristics from Cl to I. Around the frequencies of the flat acoustic bands, the three
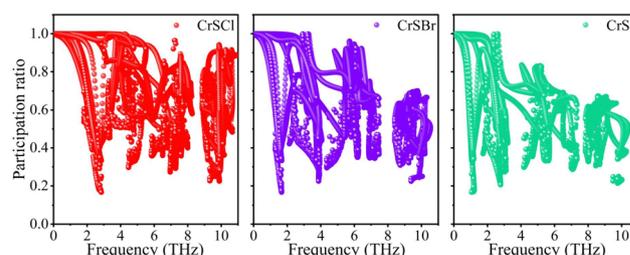

Fig. 3 Frequency resolved phonon participation ratio of CrSX monolayers.

monolayers have lower PR values, confirming rattling modes at those frequencies that arise due to localized X oscillations.

Based on the phonon transport equation, the thermal transport properties of CrSX monolayers are estimated. The κ_1 along the α direction can be determined using the following equation:

$$k_{\alpha\alpha} = \frac{1}{k_B T^2 A t N} \sum_{\lambda(k,p)} n_\lambda^0 \left(n_\lambda^0 + 1\right) (\hbar\omega_\lambda)^2 v_\lambda^\alpha v_\lambda^\alpha \tau_\lambda, \qquad (7)$$

where $\lambda(k,p)$ denotes a phonon mode with k being the wave vector and p the phonon branch number. A, t, ω, N, T, v_λ^α, n_λ^0 and τ_λ are the unit-cell area, the thickness of the unit cell, the phonon frequency, the number of q points in the first Brillouin zone (BZ) for a Γ-centered regular grid, the temperature, the phonon group velocity in the direction α, the phonon occupation number given via the Bose–Einstein distribution and the phonon relaxation time, respectively. The anisotropic κ_1 along the x and y directions for CrSX monolayers as a function temperature are shown in Fig. 4(a). At 300 K, the κ_1 are 0.624, 0.419, and 0.179 W m^{-1} K^{-1} for the x axis, and 0.193, 0.158, and 0.093 W m^{-1} K^{-1} for y axis, respectively. These values are commensurate with those of other 2D materials, such as the KAgSe monolayer (0.26 W m^{-1} K^{-1}),[54] the TlCuSe monolayer (0.44 W m^{-1} K^{-1}),[55] and the AgSbSe$_2$ monolayer (0.48 W m^{-1} K^{-1}).[56] In Fig. 4(b), the cumulative κ_1 at 300 K are shown as a function of phonon frequency. The majority of heat is conducted by acoustic and low-frequency optical phonons with phonon energy from 0 to 3 THz, while high-frequency optical phonons have almost negligible contribution to heat conduction. Cumulative κ_1 as a function of the phonon mean free path (MFP) at 300 K are shown in Fig. 4(c). Our findings reveal that, regardless of the x or y direction, the κ_1 of CrSX monolayers reach their maximum accumulation when the MFP are less than 10 nm. The smaller MFP indicates a greater scattering probability of phonons at the interface, and thereby inhibiting κ_1.[57] Eqn (7) demonstrates that the v_λ is a key

parameter in determining the κ_1 of materials. Fig. 4(d–i) show the v_λ values as a function of frequency along the x and y directions, respectively. v_λ of CrSCl, CrSBr, and CrSI decrease drastically when the frequencies converge near their respective flat-band frequencies, which are in good agreement with the flat acoustic phonon dispersion. The flat phonon dispersion indicate that the associated X atoms scatter the heat-carrying acoustic phonons, and the corresponding small group velocities lead to the lower κ_1.[58]

Another key parameter that determines the lattice thermal conductivity is the "scattering phase space (W)", which can be used as a measure of the space available for the three-phonon process allowed by the conservation of the energy. This parameter is related to the phonon frequency in ref. 59:

$$W_\lambda^\pm = \frac{1}{2N} \sum_{\lambda' p''} \left\{ \begin{array}{c} 2\left(n_0' - n_0''\right) \\ n_0' + n_0'' + 1 \end{array} \right\} \frac{\delta(\omega_\lambda \pm \omega_{\lambda'} - \omega_{\lambda''})}{\omega_\lambda \omega_{\lambda'} \omega_{\lambda''}}, \qquad (8)$$

where (+) and (−) correspond to the absorption and emission processes, respectively. Fig. 5(a–c) display the scattering phase space of the ZA, TA, LA and Optical modes for CrSX monolayers, respectively. The larger W provides more space for the three-phonon scattering process, which is a good sign of shorter phonon relaxation time (τ_λ) and lower lattice thermal conductivity.[60–63] Apparently, the ZA mode of the CrSX monolayers exhibits larger W of acoustic modes, which further suggests that it has stronger three-phonon scattering and shorter τ_λ. As analyzed in W, the ZA mode possesses a lower τ_λ, as shown in Fig. 5(d–f). The strength of the three-phonon scattering process depends on the anharmonicities of the systems, which is a crucial feature to be analyzed. Greater anharmonicities result in stronger phonon–phonon interactions, leading to lower τ_λ and κ_1. The Grüneisen parameters (γ_λ)[64] quantify the anharmonicities of crystal structures and are determined by the following equation,

$$\gamma_\lambda = -\frac{1}{6\omega_\lambda^2} \sum_{ijk\alpha\beta\gamma} \frac{\varepsilon_{i\alpha}^{\lambda*} \varepsilon_{i\beta}^\lambda}{\sqrt{M_i M_j}} r_k^\gamma \Phi_{ijk}^{\alpha\beta\gamma} e^{ik \cdot r_j}, \qquad (9)$$
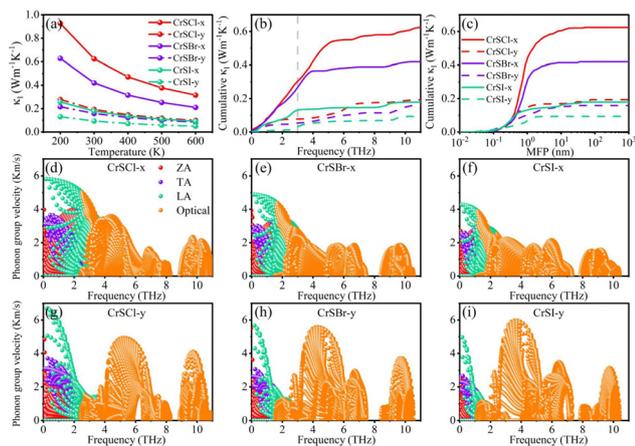

Fig. 4 (a) The κ_1 of CrSX monolayers as a function of temperature. (b) Cumulative κ_1 as a function of frequency at 300 K. (c) Cumulative κ_1 as a function of the phonon mean free path (MFP) at 300 K. (d)–(i) Phonon group velocity as a function of frequency along the x and y directions for the CrSX monolayers.
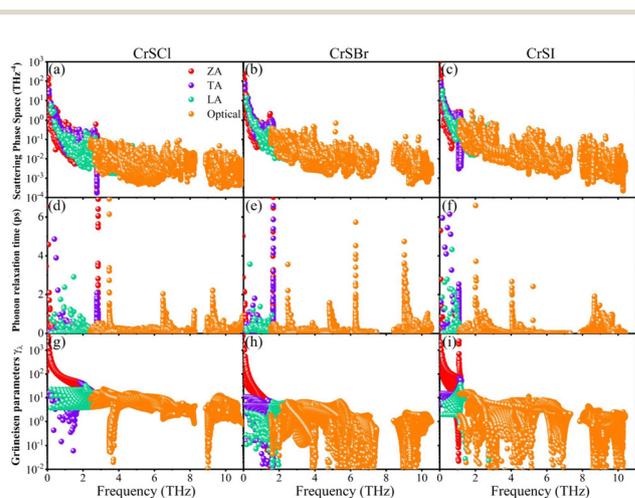

Fig. 5 (a)–(c) phonon scattering phase space, (d)–(f) phonon relaxation time, and (g)–(i) Grüneisen parameters of ZA, TA, LA and optical modes in CrSX monolayers.
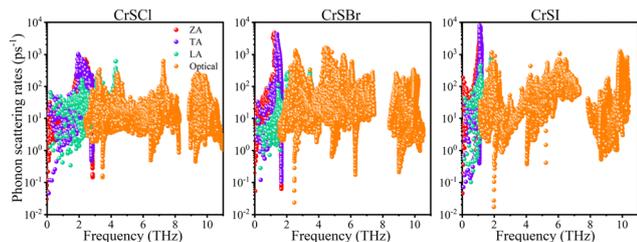
Fig. 6 Phonon scattering rates as a function of frequency for the CrSX monolayers.

where α, β and γ are the Cartesian components; i, j, and k denote atomic indices. M_i, $\varepsilon_{i\alpha}^\lambda$, r_i and $\Phi_{ijk}^{\alpha\beta\lambda}$ are the mass of atom i, the phonon eigenvector for atom i in the direction α, the position vector of the ith atom and the third-order anharmonic IFCs, respectively. Fig. 5(g–i) show the Grüneisen parameters of the ZA, TA, LA and optical modes in CrSX monolayers. Obviously, the ZA mode of CrSX monolayers has the largest γ_λ, suggesting the presence of strong anharmonicity and phonon–phonon scattering leading to short τ_λ and small κ_l. The ZA mode with the largest γ_λ may originate from the rattling vibration of the X atoms around frequencies of flat acoustic bands. Apart from the above parameters, phonon scattering rates [Fig. 6] is another major factor in determining κ_l. CrSX monolayers exhibit a remarkably high scattering rates, resulting in a shortened τ_λ and consequently, strong anharmonicity. The significant scattering rates are attributed to the abundance of scattering channels facilitated by the large W, and anharmonic phonon scattering plays a crucial role in reducing κ_l.

3.2 Electronic structure and electrical transport

The thermoelectric (TE) properties rely on low κ_l and favorable electrical transport properties, which are primarily influenced by the electronic structures. Fig. 7 displays the electron band structures of CrSX monolayers obtained through HSE06 hybrid functionals. Calculation results indicate that CrSCl, CrSBr, and CrSI monolayers are indirect bandgap semiconductors with bandgaps of 1.80, 1.69, and 1.26 eV, respectively. The conduction band minimum (CBM) and valence band maximum (VBM) are located at the X and Γ points, respectively. The CBM of CrSX monolayers exhibits highly degenerate and nearly flat dispersion along Γ–X, contributing to a higher electron effective mass
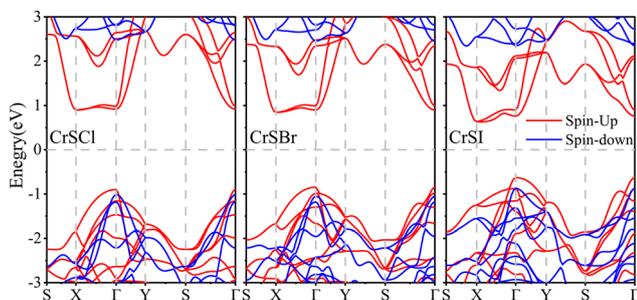

Fig. 7 The electronic band structures calculated by HSE06 hybrid functionals for CrSX monolayers, and the Fermi level is set to zero.

and increased n-type Seebeck coefficients, while a large effective mass will lead to a small carrier mobility. Consequently, the conduction bands with high dispersion along Γ–Y will exhibit a smaller effective mass and a higher carrier mobility. The dispersion of VBM for CrSCl and CrSBr along Γ–X is smaller than that along Γ–Y, whereas CrSI exhibits the opposite trend, with a larger dispersion along Γ–X compared to Γ–Y. This trend can be attributed to the varying orbital contributions to the VBM at the Γ point. From X = Cl to I, the contribution of the S atom decreases, while the contribution of the X atoms increases.[28]

We calculate the anisotropic carrier mobility (μ_{2D}) and electron relaxation time (τ) of CrSX monolayers employing the modified deformation potential approximation (DPA) method.[65]

$$\mu_x = \frac{e\hbar^3}{k_B T (m_x)^{\frac{3}{2}}(m_y)^{\frac{1}{2}}} \left(\frac{A + B - \sqrt{A^2 - B^2}}{B\sqrt{A^2 - B^2}} \right)$$
$$\times \left(\frac{I + J - \sqrt{I^2 - J^2}}{J\sqrt{I^2 - J^2}} \right), \quad (10)$$

$$\tau_x = \frac{\mu_x m_x^*}{e}, \quad (11)$$

where $A = \bar{E}_1^2 + \frac{(\Delta E_1)^2}{2}$, $B = \bar{E}_1 \Delta E_1$, $I = \frac{1}{\sqrt{\bar{C}^2 - (\Delta C)^2}}$, $J = \frac{\bar{C}}{\Delta C}\left(\frac{1}{\bar{C}} - \frac{1}{\sqrt{\bar{C}^2 - (\Delta C)^2}} \right)$ with $\bar{E}_1^2 = \frac{E_{1y} + E_{1x}}{2}$, $\Delta E_1 = \frac{E_{1y} - E_{1x}}{2}$, $\bar{C} = \frac{C_x + C_y}{2}$ and $\Delta C = \frac{C_y - C_x}{2}$. k_B, E_1, C and m^* are the Boltzmann constant, the reduced Planck constant, the deformation-potential constant, the elastic constants and the effective mass, respectively. The m^*, E_1 and C can be given by[66] $m^* = \hbar^2/(\partial^2 E/\partial k^2)$, $E_1 = \partial E_{edge}/\partial(\Delta a/a_0)$ and $C = [\partial^2 E/\partial(\Delta a/a_0)^2]/S_0$, where S_0, E, E_{edge} and $\Delta a/a_0$ are the cell area, the total energy, the shift of the VBM and CBM, and the lattice dilation, respectively. Calculated m^*, E_1, C, μ_{2D} and τ along x and y directions using DPA theory are shown in Table S3 (ESI†). According to the modified deformation potential approximation theory, both μ_{2D} and τ depend not only on the elastic constants and the deformation potential energy along the direction of carrier transport, but also on the values perpendicular to their directions.

The values of m^*, E_1, C, τ, and μ_{2D} were calculated and are summarized in Table 1, showing overall consistency with literature values.[28] The m^* values along the x-direction on the VBM (CBM) of CrSCl and CrSBr are 10–100 times greater than those along the y-direction. The m^* along the y-direction is greater than that along the x-direction at the VBM of CrSI, consistent with band structure analysis. Similarly to CrSCl and CrSBr, the CBM of CrSI also shows a larger m^* along the x-direction compared to the y-direction. μ_{2D} is inversely proportional to m^*, exhibiting an opposite trend. Furthermore, the multiplication of m^* and μ_{2D} results in weak anisotropy of τ. The electronic transport coefficients of CrSX monolayers as a function of chemical potential (μ) at 300 K, 400 K, and 500 K are shown in Fig. 8(a–l). The magnitude of $|S|$ initially increases

Table 1 Effective mass (m^*, m_0), deformation potential constant (E_1, eV), 2D elastic modulus (C, J m^{-2}), electron relaxation time (τ, fs) and carrier mobility (μ_{2D}, cm^2 V^{-1} s^{-1}) of CrSX monolayers at 300 K using a modified DPA method

| Name	Type	Direction	m^*	C	E_1	τ	μ_{2D}
CrSCl	h	$\Gamma-X$	6.554	81.1	3.42	97.792	26.243
		$\Gamma-Y$	0.080	101.0	4.63	88.940	1955.372
	e	$\Gamma-X$	5.982	81.1	5.00	32.062	9.427
		$\Gamma-Y$	0.343	101.0	4.52	35.621	182.657
CrSBr	h	$\Gamma-X$	7.118	77.1	3.03	123.511	30.519
		$\Gamma-Y$	0.091	98.8	3.51	122.068	2359.297
	e	$X-\Gamma$	7.962	77.1	4.51	24.610	5.436
		$X-S$	0.478	98.8	4.81	25.355	93.295
CrSI	h	$\Gamma-X$	0.280	73.7	7.29	30.983	194.620
		$\Gamma-Y$	4.888	96.9	1.28	62.733	22.573
	e	$X-\Gamma$	3.987	73.7	4.01	50.456	22.258
		$X-S$	0.300	96.9	4.61	50.399	295.477
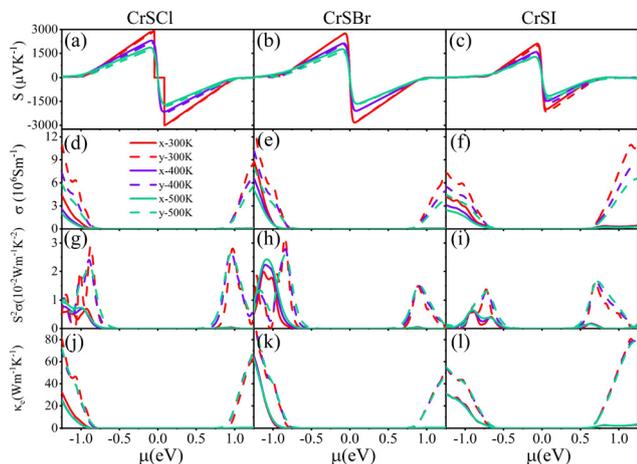
Fig. 8 The electron transport coefficients of CrSX monolayers as a function of chemical potential (μ) at 300, 400 and 500 K. (a)–(c) Seebeck coefficients (S), (d)–(f) electrical conductivity (σ), (g)–(i) power factor ($S^2\sigma$) and (j)–(l) electronic thermal conductivity (κ_e).

and then decreases with increasing magnitude of chemical potential $|\mu|$. The Seebeck coefficient decreases with increasing temperature for a given μ, which can be attributed to the concurrent increase in carrier concentration as the temperature rises. The maximum S values for CrSCl, CrSBr and CrSI monolayers at 300 K are 3009, 2802 and 2172 μV K^{-1}, respectively. The strong overlaps of the electronic group velocities cause S to nearly overlap in both directions.[67] Fig. 8(d–f) show the electrical conductivity σ increases with the increasing $|\mu|$ and decrease with temperature due to more frequent scattering of carriers at high temperatures.[68] In p-type systems, σ exhibits weak anisotropy, while in n-type systems, it shows strong anisotropy. Regardless of the doping type (p-type or n-type), σ is greater along the y direction than along the x direction. Observation from Fig. 8(g–i) reveals that $S^2\sigma$ initially increases and then decreases with increasing $|\mu|$. However, the temperature variation does not significantly affect the change in $S^2\sigma$. The optimal $S^2\sigma$ values of CrSX monolayers are consistently higher along the y direction compared to the x direction, at a given μ, due to the difference in σ. At 300 K, the maximum $S^2\sigma$

values of CrSX monolayers surpass the corresponding optimal values of T-HfSe$_2$[41] (2.92 mW mK^{-2}), T-MoS2[69] (0.07mW mK^{-2}), GeAs2[70] (3.8 mW mK^{-2}), and PbTe[70] (2.5 mW mK^{-2}), with values of 8.85, 9.53, and 4.22 mW mK^{-2}, respectively. Fig. 8(j–l) display the κ_e values of CrSX monolayers. Since κ_e is determined using the Wiedemann–Franz law, it demonstrates similar behavior to σ.

3.3 Thermoelectric figure of merit

The ZT values of CrSX monolayers at different temperatures (300 K, 400 K, and 500 K) and varying chemical potentials along the x and y directions are shown in Fig. 9. The ZT value initially increases, then decreases with increasing $|\mu|$ for both p-type and n-type doping along the x and y directions, while it increases with temperature. The significant disparity in σ contributes to a marked differentiation in the ZT values in both directions. Table 2 presents the thermoelectric parameters corresponding to the optimum ZT values at room temperature. The optimal ZT values for CrSX monolayers are 1.33, 1.18, and 2.13 along the x-axis and 5.23, 5.84, and 5.22 along the y-axis. Thus, CrSX monolayers, characterized by their remarkably high ZT values, hold tremendous potential for thermoelectric applications and can be compared to the following excellent materials. For instance, SnSe has been reported to have a low thermal conductivity (0.25 W m^{-1} K^{-1}) and a large ZT value of (2.6 ± 0.3)
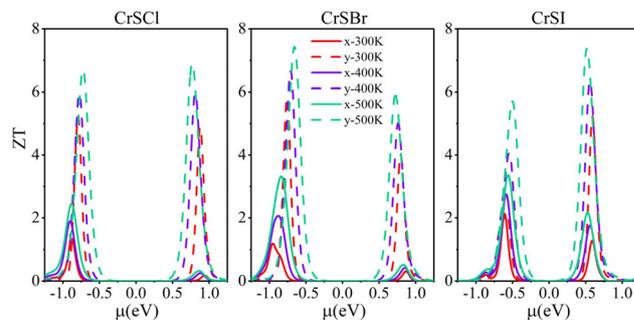

Fig. 9 ZT along the x and y directions as a function of chemical potential at 300, 400 and 500 K.

Table 2 The calculated optimum figure of merit (ZT) and Seebeck coefficients S (μV K^{-1}), electrical conductivity σ (10^5 S m^{-1}), power factor $S^2\sigma$ (10^{-2} W m^{-1} K^{-2}) and electronic thermal conductivity κ_e (W m^{-1} K^{-1}) at 300 K

Name	Type	Direction	S	σ	$S^2\sigma$	κ_e	ZT
CrSCl	h	X	277.69	0.63	0.48	0.46	1.33
		Y	454.29	0.43	0.88	0.32	5.23
	e	X	−208.05	0.10	0.04	0.07	0.18
		Y	−442.38	0.44	0.84	0.31	4.90
CrSBr	h	X	187.35	2.72	0.95	2.00	1.18
		Y	476.80	0.37	0.83	0.27	5.84
	e	X	−213.97	0.11	0.05	0.08	0.31
		Y	−412.79	0.29	0.50	0.21	4.00
CrSI	h	X	333.25	0.22	0.24	0.16	2.13
		Y	310.40	0.16	0.15	0.12	2.17
	e	X	−281.11	0.16	0.13	0.12	1.27
		Y	−455.38	0.23	0.42	0.15	5.22

at 935 K[71]. The 2D superlattice-monolayer structure (SLM) of $ZrSe_2/HfSe_2$ theoretically exhibits a ZT value of 5.3 at room temperature.[57] Moreover, the ZT value of the $Fe_2V_{0.8}W_{0.2}$ Al film can reach 5 within the temperature range of 300–400 K.[72]

4 Conclusions

In this paper, by using the density functional theory and Boltzmann transport methods, we investigated the thermal and electrical transport properties of CrSX monolayers. The lattice thermal conductivity (κ_l) values of CrSX monolayers along the x-axis are 0.624, 0.419, and 0.179 W m^{-1} K^{-1}, while along the y-axis, the values are 0.193, 0.158, and 0.093 W m^{-1} K^{-1} at room temperature. These ultralow κ_l values can be attributed to the strong anharmonicity in CrSX monolayers, which leads to small phonon relaxation times and flat acoustic phonon dispersions. The X atoms in CrSX monolayers serve as generalized rattlers in the direction perpendicular to the Cr–X–Cr plane, contributing to the strong anharmonicity. The interplay between harmonic and anharmonic phonon properties was responsible for the initial increase and subsequent decrease of the lattice thermal conductivity with the atomic mass from Cl to I. Additionally, we found that the optimum ZT values in CrSX monolayers can reach 1.33 (5.23), 1.18 (5.84) and 2.13 (5.22) along the y-axis at 300 K. The combination of ultralow lattice thermal conductivity and high figure of merit in CrSX monolayers not only highlights the potential of this system as an efficient 2D thermoelectric material but also provides valuable insights for discovering and designing high-ZT thermoelectric materials featuring rattling vibrational atoms.

Author contributions

Xiaowei Xuan conceptualized the study, conducted the DFT calculations, acquired the data, analyzed the results, and wrote the paper. Zhaoyu Yang, Rui Du, and Yimeng Zhao provided helpful discussion. Guangbiao Zhang, Yuli Yan, Chang Liu, and Hang Li initiated and designed the methodology of this work. All authors conceived the DFT calculations, analyzed the results, and coedited the manuscript.

Conflicts of interest

The authors declare that they have no known competing financial interests or personal relationships that could have appeared to influence the work reported in this paper.

Acknowledgements

Notes and references

1 J. Yang, L. Xi, W. Qiu, L. Wu, X. Shi, L. Chen, J. Yang, W. Zhang, C. Uher and D. J. Singh, *npj Comput. Mater.*, 2016, **2**, 1–17.

2 Z. Ding, M. An, S. Mo, X. Yu, Z. Jin, Y. Liao, K. Esfarjani, J.-T. Lü, J. Shiomi and N. Yang, *J. Mater. Chem. A*, 2019, **7**, 2114–2121.

3 N. Wang, H. Gong, Z. Sun, C. Shen, B. Li, H. Xiao, X. Zu, D. Tang, Z. Yin, X. Wu, H. Zhang and L. Qiao, *ACS Appl. Energy Mater.*, 2021, **4**, 12163–12176.

4 S. Chu, Y. Cui and N. Liu, *Nat. Mater.*, 2016, **16**, 16–22.

5 L.-D. Zhao, C. Chang, G. Tan and M. G. Kanatzidis, *Energy Environ. Sci.*, 2016, **9**, 3044–3060.

6 D. Li, K. Lee, B. Y. Wang, M. Osada, S. Crossley, H. R. Lee, Y. Cui, Y. Hikita and H. Y. Hwang, *Nature*, 2019, **572**, 624–627.

7 Z. Wang, L. Zhao, K. F. Mak and J. Shan, *Nano Lett.*, 2017, **17**, 740–746.

8 L.-P. Tang, L.-M. Tang, H. Geng, Y.-P. Yi, Z. Wei, K.-Q. Chen and H.-X. Deng, *Appl. Phys. Lett.*, 2018, **112**, 012101.

9 B. Poudel, Q. Hao, Y. Ma, Y. Lan, A. Minnich, B. Yu, X. Yan, D. Wang, A. Muto, D. Vashaee, X. Chen, J. Liu, M. S. Dresselhaus, G. Chen and Z. Ren, *Science*, 2008, **320**, 634–638.

10 V. Kocevski and C. Wolverton, *Chem. Mater.*, 2017, **29**, 9386–9398.

11 M. Dutta, K. Pal, M. Etter, U. V. Waghmare and K. Biswas, *J. Am. Chem. Soc.*, 2021, **143**, 16839–16848.

12 U. Aseginolaza, R. Bianco, L. Monacelli, L. Paulatto, M. Calandra, F. Mauri, A. Bergara and I. Errea, *Phys. Rev. B*, 2019, **100**, 214307.

13 J. Zhang, N. Roth, K. Tolborg, S. Takahashi, L. Song, M. Bondesgaard, E. Nishibori and B. B. Iversen, *Nat. Commun.*, 2021, **12**, 6709.

14 J. Hansson, T. M. J. Nilsson, L. Ye and J. Liu, *Int. Mater. Rev.*, 2018, **63**, 22–45.

15 D. Li, J. He, G. Ding, Q. Tang, Y. Ying, J. He, C. Zhong, Y. Liu, C. Feng, Q. Sun, H. Zhou, P. Zhou and G. Zhang, *Adv. Funct. Mater.*, 2018, **28**, 1801685.

16 X.-K. Chen, J. Liu, Z.-X. Xie, Y. Zhang, Y.-X. Deng and K.-Q. Chen, *Appl. Phys. Lett.*, 2018, **113**, 121906.

17 D. Dangić, O. Hellman, S. Fahy and I. Savić, *npj Comput. Mater.*, 2021, **7**, 57.

18 M. K. Jana, K. Pal, A. Warankar, P. Mandal, U. V. Waghmare and K. Biswas, *J. Am. Chem. Soc.*, 2017, **139**, 4350–4353.

19 J. He, M. Amsler, Y. Xia, S. S. Naghavi, V. I. Hegde, S. Hao, S. Goedecker, V. Ozoliņš and C. Wolverton, *Phys. Rev. Lett.*, 2016, **117**, 046602.

20 Z. Feng, Y. Fu, Y. Zhang and D. J. Singh, *Phys. Rev. B*, 2020, **101**, 064301.

21 X. Ye, Z. Feng, Y. Zhang, G. Zhao and D. J. Singh, *Phys. Rev. B*, 2022, **105**, 104309.

22 B. Sales, B. Chakoumakos, D. Mandrus and J. Sharp, *J. Solid State Chem.*, 1999, **146**, 528–532.

23 R. Guo, X. Wang, Y. Kuang and B. Huang, *Phys. Rev. B: Condens. Matter Mater. Phys.*, 2015, **92**, 115202.

24 X.-L. Zhu, P.-F. Liu, G. Xie, W.-X. Zhou, B.-T. Wang and G. Zhang, *Nanomaterials*, 2019, **9**, 597.

25 D. Li, Y. Gong, Y. Chen, J. Lin, Q. Khan, Y. Zhang, Y. Li, H. Zhang and H. Xie, *Nano-Micro Lett.*, 2020, **12**, 36.

26 Y. Bai, Y. Wu, C. Jia, L. Hou and B. Wang, *Appl. Phys. Lett.*, 2023, **123**, 012401.

27 B. Wang, Y. Wu, Y. Bai, P. Shi, G. Zhang, Y. Zhang and C. Liu, *Nanoscale*, 2023, **15**, 13402–13410.

28 Y. Guo, Y. Zhang, S. Yuan, B. Wang and J. Wang, *Nanoscale*, 2018, **10**, 18036–18042.

29 J. P. Perdew and A. Zunger, *Phys. Rev. B: Condens. Matter Mater. Phys.*, 1981, **23**, 5048–5079.

30 P. E. Blöchl, *Phys. Rev. B: Condens. Matter Mater. Phys.*, 1994, **50**, 17953–17979.

31 G. Kresse and D. Joubert, *Phys. Rev. B: Condens. Matter Mater. Phys.*, 1999, **59**, 1758–1775.

32 J. Heyd, G. E. Scuseria and M. Ernzerhof, *J. Chem. Phys.*, 2003, **118**, 8207–8215.

33 A. Togo and I. Tanaka, *Scr. Mater.*, 2015, **108**, 1–5.

34 L. Chaput, A. Togo, I. Tanaka and G. Hug, *Phys. Rev. B: Condens. Matter Mater. Phys.*, 2011, **84**, 094302.

35 W. Li, J. Carrete, N. A. Katcho and N. Mingo, *Comput. Phys. Commun.*, 2014, **185**, 1747–1758.

36 G. K. H. Madsen and D. J. Singh, *Comput. Phys. Commun.*, 2006, **175**, 67–71.

37 J. C. Klöckner, M. Matt, P. Nielaba, F. Pauly and J. C. Cuevas, *Phys. Rev. B*, 2017, **96**, 205405.

38 G. J. Snyder and E. S. Toberer, *Nat. Mater.*, 2008, **7**, 105–114.

39 S. Tang, S. Bai, M. Wu, D. Luo, D. Wang, S. Yang and L.-D. Zhao, *Mater. Today Energy*, 2022, **23**, 100914.

40 W. Fang, H. Wei, X. Xiao, Y. Chen, M. Li and Y. He, *ACS Appl. Energy Mater.*, 2022, **5**, 7802–7812.

41 G. Ding, G. Y. Gao, Z. Huang, W. Zhang and K. Yao, *Nanotechnology*, 2016, **27**, 375703.

42 R. Hill, *Proc. Phys. Soc., London, Sect. A*, 1952, **65**, 349.

43 A. Reuss, *Z. Angew. Math. Mech.*, 1929, **9**, 49–58.

44 O. L. Anderson, *J. Phys. Chem. Solids*, 1963, **24**, 909–917.

45 M. Maździarz, *2D Mater.*, 2019, **6**, 048001.

46 W. Qiu, L. Xi, P. Wei, X. Ke, J. Yang and W. Zhang, *Proc. Natl. Acad. Sci. U. S. A.*, 2014, **111**, 15031–15035.

47 W. Lai, Y. Wang, D. T. Morelli and X. Lu, *Adv. Funct. Mater.*, 2015, **25**, 3648–3657.

48 J. Wang, Z. Huang, W. Liu, C. Chang, H. Tang, Z. Li, W. Chen, C. Jia, T. Yao, S. Wei, Y. Wu and Y. Li, *J. Am. Chem. Soc.*, 2017, **139**, 17281–17284.

49 A. Lou, Q.-B. Liu and H.-H. Fu, *Phys. Rev. B*, 2022, **105**, 075431.

50 H. H. Huang, X. Fan, D. J. Singh and W. T. Zheng, *J. Mater. Chem. C*, 2019, **7**, 10652–10662.

51 J. Hafner and M. Krajci, *J. Phys.: Condens. Matter*, 1993, **5**, 2489.

52 S. Lu, Y. Ouyang, C. Yu, P. Jiang, J. He and J. Chen, *J. Appl. Phys.*, 2021, **129**, 225106.

53 Z. Zhang, S. Hu, Q. Xi, T. Nakayama, S. Volz, J. Chen and B. Li, *Phys. Rev. B*, 2020, **101**, 081402.

54 X.-L. Zhu, H. Yang, W.-X. Zhou, B. Wang, N. Xu and G. Xie, *ACS Appl. Mater. Interfaces*, 2020, **12**, 36102–36109.

55 W. Lin, J. He, X. Su, X. Zhang, Y. Xia, T. P. Bailey, C. C. Stoumpos, G. Tan, A. J. E. Rettie, D. Y. Chung, V. P. Dravid, C. Uher, C. Wolverton and M. G. Kanatzidis, *Adv. Mater.*, 2021, **33**, 2104908.

56 M. D. Nielsen, V. Ozolins and J. P. Heremans, *Energy Environ. Sci.*, 2013, **6**, 570–578.

57 G. Ding, C. Wang, G. Gao, K. Yao, C. Dun, C. Feng, D. Li and G. Zhang, *Nanoscale*, 2018, **10**, 7077–7084.

58 X. Jiang, Z. Zhang, Z. Liu, J. Wang and Y. Liu, *Appl. Phys. Lett.*, 2022, **120**, 132202.

59 W. Li and N. Mingo, *Phys. Rev. B: Condens. Matter Mater. Phys.*, 2015, **91**, 144304.

60 T. Pandey and A. K. Singh, *J. Mater. Chem. C*, 2016, **4**, 1979–1987.

61 T. Pandey, C. A. Polanco, L. Lindsay and D. S. Parker, *Phys. Rev. B*, 2017, **95**, 224306.

62 T. Tadano, Y. Gohda and S. Tsuneyuki, *Phys. Rev. Lett.*, 2015, **114**, 095501.

63 L. Lindsay, *Nanoscale Microscale Thermophys. Eng.*, 2016, **20**, 67–84.

64 D. A. Broido, A. Ward and N. Mingo, *Phys. Rev. B: Condens. Matter Mater. Phys.*, 2005, **72**, 014308.

65 H. Lang, S. Zhang and Z. Liu, *Phys. Rev. B*, 2016, **94**, 235306.

66 J. Bardeen and W. Shockley, *Phys. Rev.*, 1950, **80**, 72–80.

67 N. T. Hung, A. R. T. Nugraha and R. Saito, *Appl. Phys. Lett.*, 2017, **111**, 092107.

68 N. Wang, M. Li, H. Xiao, X. Zu and L. Qiao, *Phys. Rev. Appl.*, 2020, **13**, 024038.

69 Y. Xie, T.-M. Chou, W. Yang, M. He, Y. Zhao, N. Li and Z.-H. Lin, *Semicond. Sci. Technol.*, 2017, **32**, 044003.

70 A. Hassan, Y. Guo, Q. Wang, Y. Kawazoe and P. Jena, *J. Appl. Phys.*, 2019, **125**, 065308.

71 L.-D. Zhao, S.-H. Lo, Y. Zhang, H. Sun, G. Tan, C. Uher, C. Wolverton, V. P. Dravid and M. G. Kanatzidis, *Nature*, 2014, **508**, 373–377.

72 B. Hinterleitner, I. Knapp, M. Poneder, Y. Shi, H. Müller, G. Eguchi, C. Eisenmenger-Sittner, M. Stöger-Pollach, Y. Kakefuda, N. Kawamoto, Q. Guo, T. Baba, T. Mori, S. Ullah, X.-Q. Chen and E. Bauer, *Nature*, 2019, **576**, 85–90.